The Bias of Molecular Clump Identification Programs: the Example of the Carina Molecular Clouds

N. Schneider[A,D] *and K. Brooks*[B,C,E]

[A] OASU/L3AB, 33270 Floirac, France
[B] European Southern Observatory, Casilla 19001 Santiago, Chile
[C] Departamento de Astronomia, Universidad de Chile, Santiago, Chile
[D] E-mail: schneider@obs.u-bordeaux1.fr
[E] E-mail: kbrooks@das.uchile.cl

Abstract: A large scale ^{12}CO $J = 1 \to 0$ molecular line map of the Carina molecular cloud complex was obtained with the Mopra radio telescope in order to investigate its spatial and kinematic structure. The data show a complex velocity structure in two distinct cloud regions — the Northern and Southern Carina clouds. Two different clump identification methods (GAUSSCLUMPS and CLUMPFIND) were applied to the data. Though both algorithms find a similar clump mass spectral index (1.95 and 1.8, respectively), the properties of the clumps (mass, size, virial equilibrium) differ significantly. We discuss possible explanations for this discrepancy and question the validity of the Larson relations which could be an artifact of the limited spatial resolution and dynamic range of the observations.

Keywords: ISM: molecules — ISM: individual Carina — methods: data analysis

1 Introduction

Single stars and clusters of stars form from gravitational fragmentation of molecular cloud material (see e.g. Ward-Thompson 2002 for a recent review). There is observational evidence (Blitz & Williams 1997) that both low-mass and high-mass stars ($M > 8\,\mathrm{M}_\odot$) originate from substructures ('pre-stellar cores' or 'clumps') within Giant Molecular Clouds (GMCs, $M > 10^4\,\mathrm{M}_\odot$). The distribution of masses from which stars are formed is characterised by the stellar Initial Mass Function (IMF; Salpeter 1955). It is described by a power law $dN/dM \propto M^{-\alpha}$ with dN the number of stars in the mass interval dM and with an index α of 2.1–2.5.

A similar power law distribution but with a lower value of $\alpha \sim 1.4$–1.9 (Elmegreen & Falgarone 1996; Kramer et al. 1998) was observationally determined for the mass distribution of molecular clumps, obtained from various molecular line studies. No systematic difference between cloud types (giant, translucent, etc.) or transient gas clumps and protostellar cores (Williams & Blitz 1998) was found. However, there is no proven link between the clumpy structure of the pre-collapse cloud core and the stellar IMF.

Since a power law does not have a characteristic scale, it is tempting to describe the cloud structure in terms of fractal parameters (e.g. Elmegreen & Falgarone 1996). However, recent observations of dark clouds (Motte, André, & Neri 1998; Testi & Sargent 1998) point towards a two-step power law with a steeper mass spectrum (α around 2)

for cloud cores (masses around $1\,\mathrm{M}_\odot$) and a lower, flatter index for the larger and more massive clumps.

Numerical models of turbulent molecular clouds are available now (see Mac Low & Klessen 2004 for a recent review) which, combined with observations like those presented in this paper, can yield a more consistent picture of the processes involved when a star forms. For example, recent hydrodynamic models (Klessen et al. 1998; Klessen & Burkert 2001) show that the clump mass spectrum of protostellar cores is similar to the observed one as long as gravity is the dominating process. If turbulence takes over, the mass spectrum is steeper and approaches a Salpeter-like mass function.

Different techniques have been developed to analyse the clumpiness of molecular clouds in a systematic and automated way. One technique involves the decomposition of a molecular-line data cube into discrete clumps that are characterised by such parameters as size, linewidth, temperature, and mass. Two routines which use this technique are GAUSSCLUMPS originally developed by Stutzki & Güsten (1990) and CLUMPFIND developed by Williams et al. (1994). As Stutzki (1993) points out, these clump identification methods do not prove that the molecular cloud consists of clumps in a hierarchical structure, instead they provide a means to measure, in a more defined way, the parameters which characterise such an assumption.

Although both routines are used frequently for analysing molecular cloud structure and the investigation

of correlations in their properties (mass, size, etc.) — commonly known as the Larson relations (Larson 1981) — no detailed study of the differences between these clump finding routines has been reported. In order to investigate to what extent the identification and properties of the clumps depend on the algorithm used, we applied both routines to an extensive ^{12}CO $J = 1 \rightarrow 0$ emission map of the Carina Nebula. We derive the spectral mass function, investigate the Larson relations, and discuss the properties of the Carina cloud in comparison to other GMCs.

2 The Carina Molecular Cloud

The Carina Nebula, at a distance of 2.2 kpc, is part of a giant molecular cloud complex that extends over a projected distance of 130 pc (Grabelsky et al. 1988; Fukui et al. 1999; Zhang et al. 2001). The two most influential star clusters in the nebula are Trumpler 14 and Trumpler 16 (hereafter Tr 14 and Tr 16), which contain a combined total of more than 30 O-type stars (Feinstein 1995). Tr 16 also contains one of the most massive stars known — Eta Carina (hereafter η Car). Ages for Tr 14 and Tr 16 have been reported to be between 1 and 6×10^6 yr (e.g. Tapia et al. 2003). Such a massive stellar concentration creates an environment with a strong radiation field and prominent stellar winds. For comparison, another well-studied Galactic star-forming region like Orion is dominated by a single O6-type star. A large fraction of the Carina GMC in the vicinity of Tr 14 and Tr 16 has already been destroyed (Brooks et al. 1998, 2003). One goal of this paper is to investigate the structure of the remaining molecular material and to see if it differs from more quiescent Galactic molecular clouds.

3 Data

The ^{12}CO $J = 1 \rightarrow 0$ data were taken from the study of Brooks et al. (1998) using the Mopra 22-m Telescope, operated by the Australia Telescope National Facility, CSIRO. At that time, the effective radius of the telescope was 15-m. The data cover an area of approximately $40' \times 50'$ with a $40''$ sampling grid (the FWHM beamsize is 43 arcsec at 115 GHz). The velocity resolution is 0.16 km s^{-1} and the average rms noise determined from a signal-free channel is 0.36 K.

3.1 Clump Decomposition

3.1.1 GAUSSCLUMPS

GAUSSCLUMPS uses a least-squares fitting procedure to decompose a data cube (two coordinate axes and velocity) into series of Gaussian-shaped clumps by iteratively subtracting fitted clumps. The procedure works in a similar way to the CLEAN algorithms used in interferometric imaging techniques. The fit is achieved through minimising χ^2 with respect to the main clump parameters: peak intensity, position, spatial size, major axis, linewidth, the velocity gradient in both directions, and a constant background temperature. These parameters are constrained to

lie within certain ranges specified by a weighting function w and three stiffness parameters s_o, s_a, and s_c. (See Kramer et al. 1998 for an explanation of the parameters.) It then subtracts the fitted clump from the original map creating a residual map, which is used as the input map for the next iteration. These steps are repeated until the sum of the intensity of all the clumps matches the integrated intensity of the original map.

The procedure was applied to the ^{12}CO $J = 1 \rightarrow 0$ data cube of Carina obtained with Mopra. The cutoff diameter and the FWHM of w were set to three and six times the beamsize, respectively. The stiffness parameter combination was varied in order to minimise the residuals between the original intensity and the fitted intensity. Fits below a chosen threshold peak intensity of 1.2 K (3σ) were discarded. The optimal stiffness parameter combination (Kramer et al. 1998) was used with $s_o = 1$, $s_a = 1$, and $s_c = 1$.

3.1.2 CLUMPFIND

CLUMPFIND decomposes an observed three-dimensional data cube into a number of clumps by assigning each volume element to local peaks of emission, thus naturally restricting the total number of clumps found. It is similar to the way the eye would analyse the distribution. The peaks of emission are traced by a set of near temperature increments (contours). For the Mopra ^{12}CO $J = 1 \rightarrow 0$ data set, the increment was 1.2 K (the 3σ level of the data) in order to be consistent with GAUSSCLUMPS. The program starts with the highest contour level and progresses down to the lower levels, finding new clumps and extending previously found clumps until the final level is reached. The shape of the clumps identified is arbitrary and the clumps themselves are considered as the basic building blocks of the cloud showing normally no substructure (Williams et al. 1994).

3.2 Mass Determination

Masses were determined using the H_2 column density $N(H_2)$ [cm^{-2}] calculated from the observed ^{12}CO $J = 1 \rightarrow 0$ line integrated intensity $W_{^{12}CO}$ [K km s^{-1}]:

$$N(H_2) = 2.3 \times 10^{20} W_{^{12}CO} \qquad (1)$$

The empirical conversion factor $(2.3 \pm 0.3) \times 10^{20}$ (Dame et al. 1993; Strong et al. 1988) was found to be valid for galactic GMCs. Even though the ^{12}CO line is normally optically thick and should therefore not be a good tracer for the total column density and mass, Genzel et al. (1999) point out why this line still permits to trace reasonably well the total mass of a molecular cloud: For UV illuminated molecular clouds, low-J ^{12}CO lines are opaque in photon-dominated region (PDR) models (Kaufman et al. 1999) and origin in or close to the CO core of a cloud. The CO luminosity (L_{CO}) is independent of the UV field and for typical clump sizes (mass ranges $10 M_\odot < M < 10^4 M_\odot$) proportional to the mass. Therefore, low-J ^{12}CO lines give indeed a good lower limit to the total mass of a clump/cloud.

The individual clump masses are then obtained by

$$M \, [\text{M}_\odot] = N(\text{H}_2) \, 2m_\text{H} \mu A D^2 (\pi/180)^2 \qquad (2)$$

with $m_\text{H} = 1.67 \times 10^{-24}$ g (mass of H-atom), $\mu = 1.36$ (average molecular mass per H-atom), D the distance [pc], and A the area of the clump [deg^2]. The clumps have an effective radius R [pc] defined by $2R = \theta_\text{maj} + \theta_\text{min}$, where θ_maj and θ_min are the sizes of the major and minor axis defining the clump size. The average H_2 density is evaluated by $n(\text{H}_2)$ [cm^{-3}] $= 1.5 M/R^3$. The virial masses are determined by:

$$M_\text{vir} \, [\text{M}_\odot] = 370 R v_\text{FWHM}^2 \qquad (3)$$

with the line width v_FWHM [km s^{-1}], related to the velocity dispersion within a clump σ by

$$\sigma \, [\text{km s}^{-1}] = v_\text{FWHM}/\sqrt{(8 \log 2)}. \qquad (4)$$

All virial masses in this paper were determined assuming a Gaussian density distribution (a radial density distribution $n(r) \propto r^{-2}$ leads to $M_\text{vir} \, [\text{M}_\odot] = 126 R v_\text{FWHM}^2$).

The minimum clump mass ΔM_min (Kramer et al. 1998) in one spatial and velocity pixel which can be identified is limited by the spatial Δx_FWHM and velocity resolution Δv_res and the rms noise ΔT_rms of the data:

$$\Delta M_\text{min} \, [\text{M}_\odot] = \Delta T_\text{rms} \, \Delta x_\text{FWHM}^2 \, \Delta v_\text{res}. \qquad (5)$$

For the Mopra data set, this minimum detectable clump mass is 0.33 M$_\odot$. Considering however that only clumps above the 3σ temperature level are used having a spatial and velocity resolution larger than 150% of the respective intrinsic values, the minimum mass for a clump is 1.6 M$_\odot$.

4 Results

4.1 Large-Scale Properties

The line-integrated Mopra ^{12}CO $J = 1 \rightarrow 0$ map is shown in Fig. 1a as an overlay to a visual extinction map (Bontemps et al. 2004, in preparation) obtained with Two Micron All Sky Survey (2MASS) data and in Fig. 1b to a Midcourse Space Experiment (MSX) image (Price 1995) of the Carina Nebula corresponding to emission at A-band: $6.8-10.8 \, \mu$m ($8 \, \mu$m).

The extinction map gives an overview of the large-scale distribution of molecular gas in the Carina region. Several complexes with a filamentary structure can be identified, extending from the northwest diagonally to the southeast. A large part of this area was covered by an atomic carbon (at 492 GHz) and ^{12}CO $J = 4 \rightarrow 3$ survey from Zhang et al. (2001). The integrated ^{12}CO $J = 1 \rightarrow 0$ emission obtained with Mopra defines two major components of the central GMC: the Northern and Southern clouds. A large part of the Northern cloud curves around Tr 14 and is exposed to its strong radiation field and stellar winds. The brightest CO emission peak is adjacent to Tr 14 and several ionisation fronts (see Brooks et al. 2003). The Southern

cloud is confined to a dark dust lane which bisects the nebula at optical wavelengths. Situated between the Northern and Southern clouds is η Car and the Keyhole Nebula. Here the original molecular cloud has largely been destroyed and all that remains are several small exposed molecular clumps (Cox & Bronfman 1995; Brooks et al. 2000; Rathborne et al. 2002). The Southern Carina cloud constitutes the tips of giant mid-infrared emission pillars ('Southern Pillars') that point towards Tr 14 and Tr 16 (Smith et al. 2000; Rathborne et al. 2002) and which show up nicely in the extinction map.

In Fig. 1b, it becomes obvious that bright $8 \, \mu$m emission is prevalent throughout both the Northern and Southern clouds. In this band the emission arises from fluorescently excited polycyclic aromatic hydrocarbons (PAHs) and thermal emission from warm dust grains (150–400 K). PAHs are well-established tracers of photodissociation regions (PDRs). The brightest $8 \, \mu$m emission in the Carina Nebula arises from η Car (between the two molecular clouds). This illustrates the large extent to which the molecular gas has been exposed to far-UV (FUV) radiation from the massive stellar members of Tr 14 and Tr 16. In the northern part of the region the $8 \, \mu$m emission is much weaker suggesting that this part of the GMC remains relatively well shielded. On the other hand, discrete ^{12}CO $J = 1 \rightarrow 0$ clumps in the Southern cloud correspond to $8 \, \mu$m emission features.

4.2 Velocity Structure

The sequence of Mopra ^{12}CO $J = 1 \rightarrow 0$ images shown in Figs 2 and 3 reveals the complex large-scale velocity structure of the molecular gas. Emission from the Northern cloud covers the velocity range -30 to -8 km s^{-1} whereas emission from the Southern cloud is confined to a smaller range of -30 to $\sim$–20 km s^{-1}. Emission arising from the discrete clumps at the south-eastern edge of the map exhibits an assortment of velocity ranges.

The Southern cloud shows a substructure composed of two main emission clumps which can be identified in the image at -27.1 km s^{-1}. The main CO peak is found at RA(2000) $= 10^h 40^m 00^s$ and DEC(2000) $= -59°8'$ where Megeath et al. (1996) identified the IRAS source 10 430 (marked with a cross), the only indication for active star formation in the Southern cloud.

In contrast, the morphology of the Northern cloud is much more complex with several branches of emission containing chains of clumps. Between velocities of -30 and -23 km s^{-1} the emission arises from the western part of the cloud. As is the case for the Southern cloud, this emission corresponds to a dust lane which obscures the nebula at optical wavelengths. This is consistent with the schematic models proposed by de Graauw et al. (1981) and Brooks et al. (2003), for which the blue-shifted emission is situated in front of the nebula. The bulk of the emission in the Northern cloud is within the velocity range -17 to -21 km s^{-1}. The brightest emission arises at a velocity of -18.5 km s^{-1}, taken to be the systemic velocity of the cloud. Towards higher velocities, the emission becomes
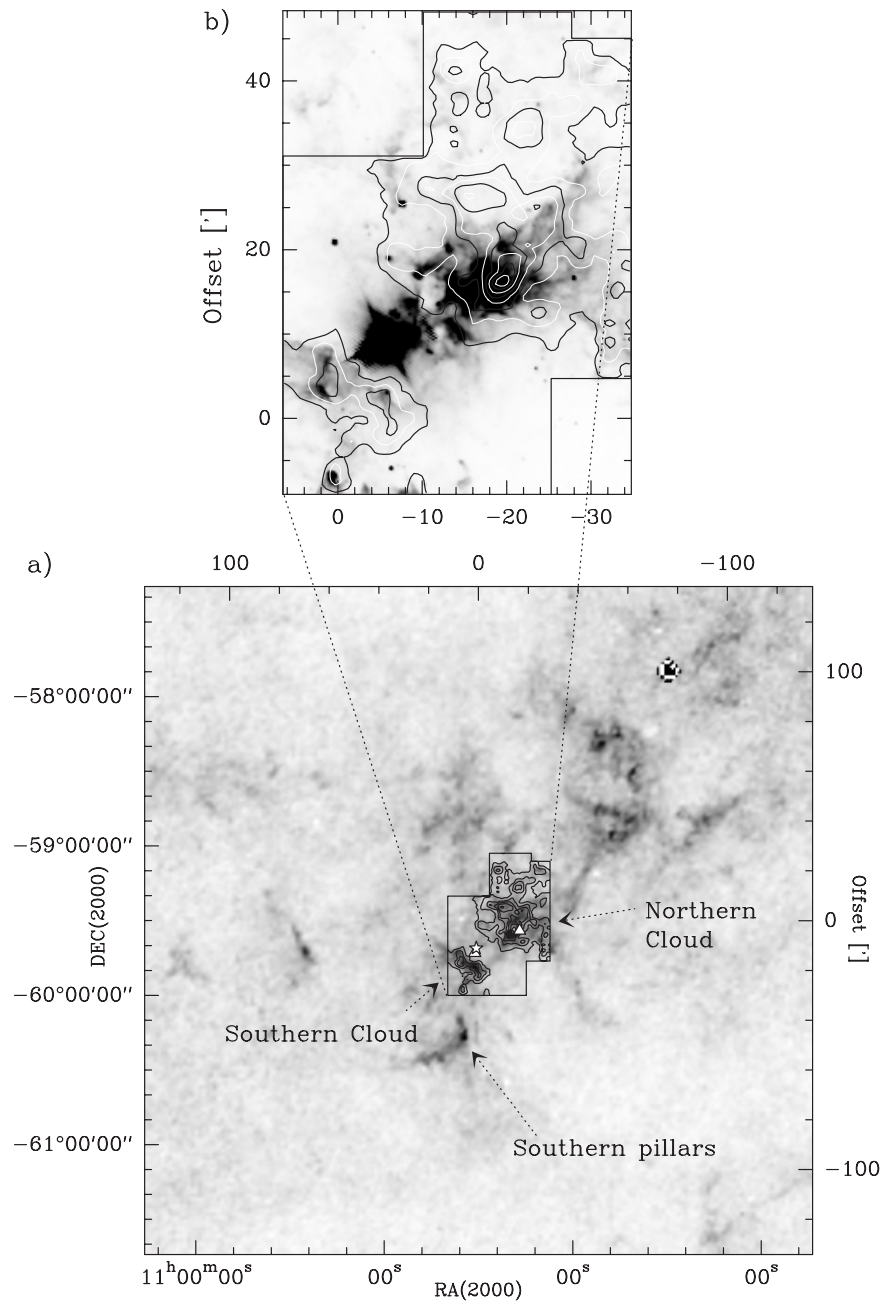
Figure 1 (a) Mopra ^{12}CO $J = 1 \rightarrow 0$ line integrated intensity map as contours, overlaid on a visual extinction map obtained from 2MASS. The contour lines are from 1 to 9 K km s^{-1} in steps of 1 K km s^{-1}. The darkest features in the extinction map are several Tens magnitudes. The star indicates η CAR, the triangles Tr 14 and Tr 16. (b) The ^{12}CO $J = 1 \rightarrow 0$ map is overlaid on an MSX A-band image.

fainter and more diffuse. According to Brooks et al. (2003) this red-shifted emission arises from the rear face of the molecular cloud.

This is the first time the Mopra ^{12}CO $J = 1 \rightarrow 0$ map has been presented in such detail. The data reveal a much more clumpy and complex structure than other large-scale maps of the region made at lower angular resolution (e.g. Zhang et al. 2001; Grabelsky et al. 1998). A recent large-scale map of ^{12}CO $J = 3 \rightarrow 2$ emission at 20″ angular resolution obtained with Atacama Submillimeter Telescope Experiment (ASTE) is shown but not discussed in Yamaguchi (2003).

In the next Section we quantify the clumpy structure using the two different clump-finding algorithms.

5 Clump Identification and Clump Mass Spectra

5.1 Results from GAUSSCLUMPS

The GAUSSCLUMPS (GC) procedure identifies approximately 2300 clumps for the Northern and Southern Carina clouds together. For the Carina clouds, the algorithm is very robust with regard to variations of the clump finding characteristics (e.g. stiffness parameters), the number of clumps found varies only by 20%. The total number is fully
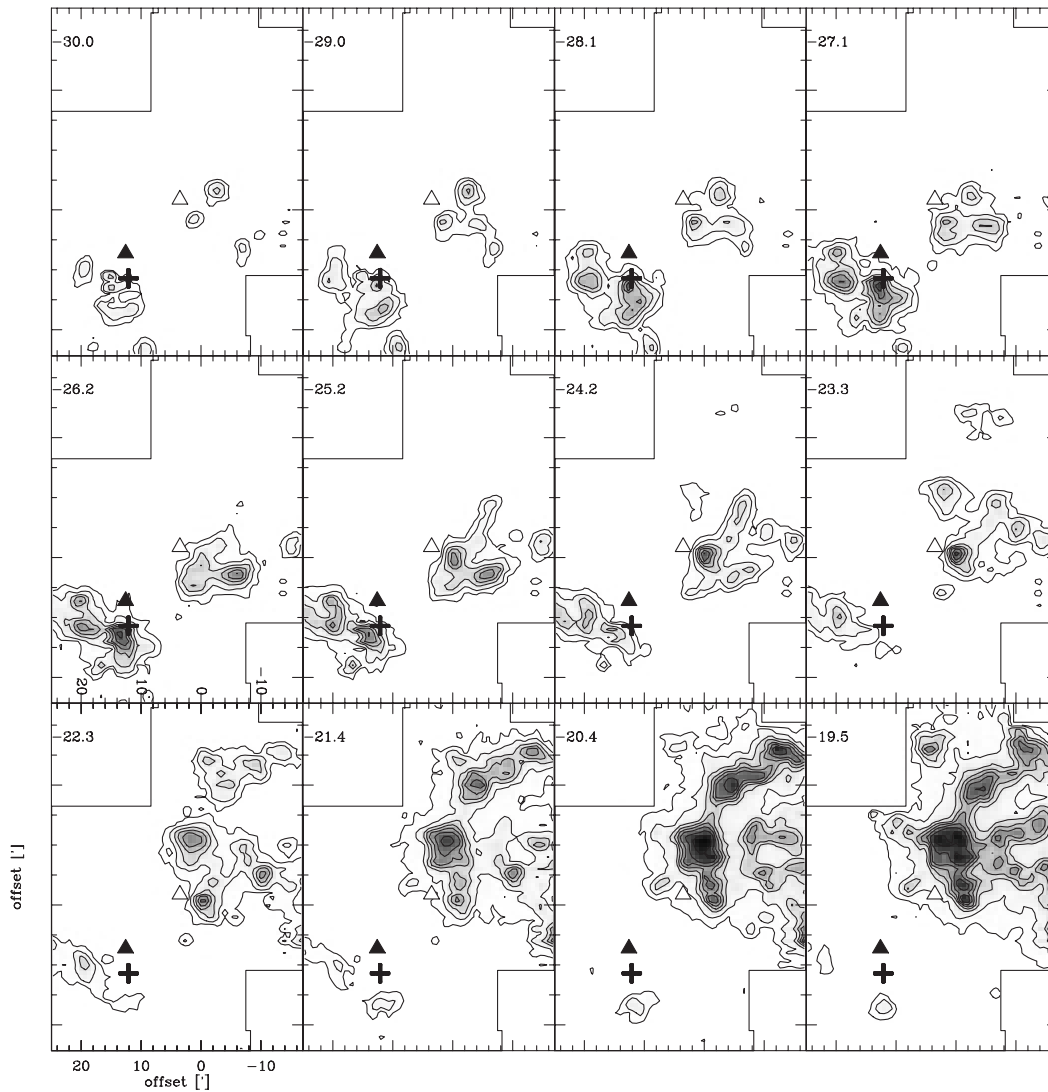
Figure 2 Channel maps (several channels are comprised) of ^{12}CO $J = 1 \to 0$ line emission in the velocity range -30 to $-19.5\,\mathrm{km\,s^{-1}}$. The cross marks the IRAS source 10 430; the triangles indicate Tr 14 (blank) and Tr 16 (filled). Contours start at $12\sigma = 4\,\mathrm{K\,km\,s^{-1}}$ and go in steps of 12σ.

accordant with values found for other regions (Kramer et al. 1998) if we compare the number of clumps found per area unit. The large number of clumps is also due to the high spatial dynamic range (ratio of mapped area to square of resolution) of around 4800. Typical values for smaller maps are a few hundred to 1500 (Kramer et al. 1998).

Figure 4 illustrates for a small velocity range (six channels) how GC is working: ellipses indicate the position of clumps in space, considering their FWHM and position angle. For the velocity axis, an ellipse is drawn in the velocity range $v_0 \pm 1.2 \times dv$ with the center velocity v_0 and dv the velocity width of the clump. Thus, one clump normally covers several channels. The majority of ellipses correspond to ^{12}CO emission but there are also some examples where no or only a weak correlation is found. This can partly be due to the fact that these clumps have a small velocity width and are thus plotted in channels without corresponding emission or they are indeed artefacts

of the fitting process. This happens particularly when the clumps have a very irregular, non-Gaussian shape (Kramer et al. 1998).

The main clump characteristics for GC are found in the first line of Table 1. The total mass of both Carina clouds derived by summing up the masses of all clumps found ($\sim$98% of the map intensity was fitted) is $133\,000\,\mathrm{M_\odot}$ which constitutes approximately one-third of the larger complex identified in the Columbia survey ($500\,000\,\mathrm{M_\odot}$). The lightest clumps have masses around $2\,\mathrm{M_\odot}$, which is just above the minimum detectable mass.

5.2 Results from CLUMPFIND

The CLUMPFIND (CF) procedure identifies only 230 clumps, a factor of ten smaller than what was found with GC. This is not surprising since the algorithm limits the total number of clumps to the number of local maxima identified in the original data cube, thus probably
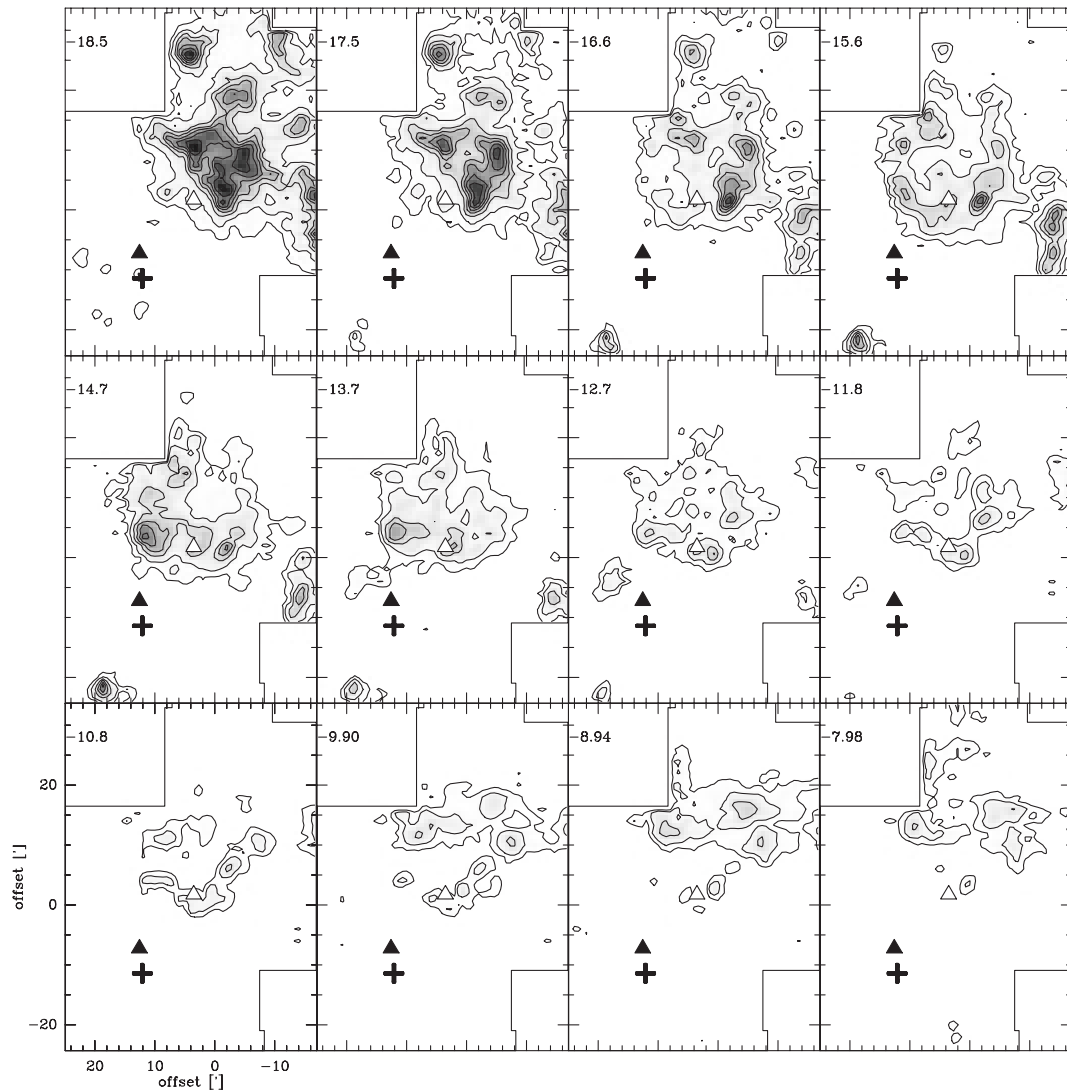
Figure 3 Channel maps of ^{12}CO $J = 1 \rightarrow 0$ line emission in the velocity range -18.5 to $-8\,\mathrm{km\,s^{-1}}$. Contouring is identical to Fig. 2. The cross marks the IRAS source 10430; the triangles indicate Tr 14 (blank) and Tr 16 (filled).

assigning much of the small scale emission to substructure of the largest clumps found (Williams et al. 1994). The clump with the lowest mass has a mass of already $4\,\mathrm{M_\odot}$, a factor of two higher than the lightest GC clump. However, the most massive clump found with CF has a mass of $5470\,\mathrm{M_\odot}$, which is half of the most massive ($10\,000\,\mathrm{M_\odot}$) clump found with GC. However, in our sample, the very massive GC clump is more extended and has a larger velocity dispersion ($3.7\,\mathrm{km\,s^{-1}}$) than the clumps found by CF at the same location. (For these clumps, the velocity dispersion is typically $<2\,\mathrm{km\,s^{-1}}$.)

5.3 The Clump Mass Spectrum

From the number of clumps $\mathrm{d}N$ within a mass interval $\mathrm{d}M$, the clump mass distribution $\mathrm{d}N/\mathrm{d}M \propto M^{-\alpha}$ is determined. In Fig. 5, we plot $\log(\mathrm{d}N)$ against $\log(\mathrm{d}M)$ for the clumps identified with GC (left) and CF (right), so that the slope of this curve directly gives the clump mass spectral index α.

We see that the number of clumps gradually increases with decreasing mass until a turnover point at approximately $16\,\mathrm{M_\odot}$ ($\log M = 1.21$) for GC and $400\,\mathrm{M_\odot}$ for CF. Beyond the turnover, the number of clumps decreases again. This turnover point does not indicate the Jeans mass or the minimum detectable mass and therefore does not represent a characteristic mass but results from undersampling the clumps with the lowest masses. Therefore, the data points to the left of the turnover mass are not included in a least square fit to determine α. Errors were assumed to follow Poisson statistics. For the CF algorithms a spectral index of 1.8 is obtained and for GC the index is 1.95. We made several GC runs with other stiffness parameters and rms noise levels and found values for α between 1.85 and 1.95. Choosing a higher noise level (e.g. six times the rms noise temperature instead of three times) makes the spectrum slightly flatter because less light clumps (with masses still higher than the turnover mass) are found.

Generally, the slope is steep, indicating that a large number of low mass clumps were found. Values of 1.8 and 1.9 are at the high end of the range of typical α values (1.4–1.9; Elmegreen & Falgarone 1996; Kramer et al. 1998) but are in good accordance with e.g. the results from the Galactic Ring survey ($\alpha = 1.8$, Simon et al. 2001) and other systematic studies of extended mapping areas (Heyer & Terebey 1998; Nagahama et al. 1998). Thus it might be that the clump mass spectral index is systematically higher when determined from large to very large fields, which is probably related to the higher dynamic range of the observations (larger area, higher spatial resolution). For example, a decomposition of spatially limited $^{13}CO\ 2 \to 1$ maps of the Carina cloud cores ($5' \times 5'$ and $6.5' \times 8'$, respectively; Brooks et al. 2003) produced a flatter spectrum for both clouds.

5.4 Comparison between GAUSSCLUMPS and CLUMPFIND

The higher α index of 1.95 found by GC implies that GAUSSCLUMPS identifies a larger number of small clumps than CLUMPFIND. It was already discussed by some authors (Williams et al. 1994; Ballesteros-Paredes & Mac Low 2002) that CLUMPFIND has a tendancy to blend smaller features with the more massive ones producing a flatter mass spectrum. In the direct comparison for the Carina cloud, we find the same behaviour. In addition, the mass range found by CF is much more limited compared to GC, i.e. the turnover point already occurs at $400\,M_\odot$, although there is observational evidence that there are clumps with masses of the order of $10\,M_\odot$ separated in space and velocity (Cox & Bronfman 1995; Rathborne et al. 2002). For the Rosette Molecular cloud, Williams et al. (1995) indicate
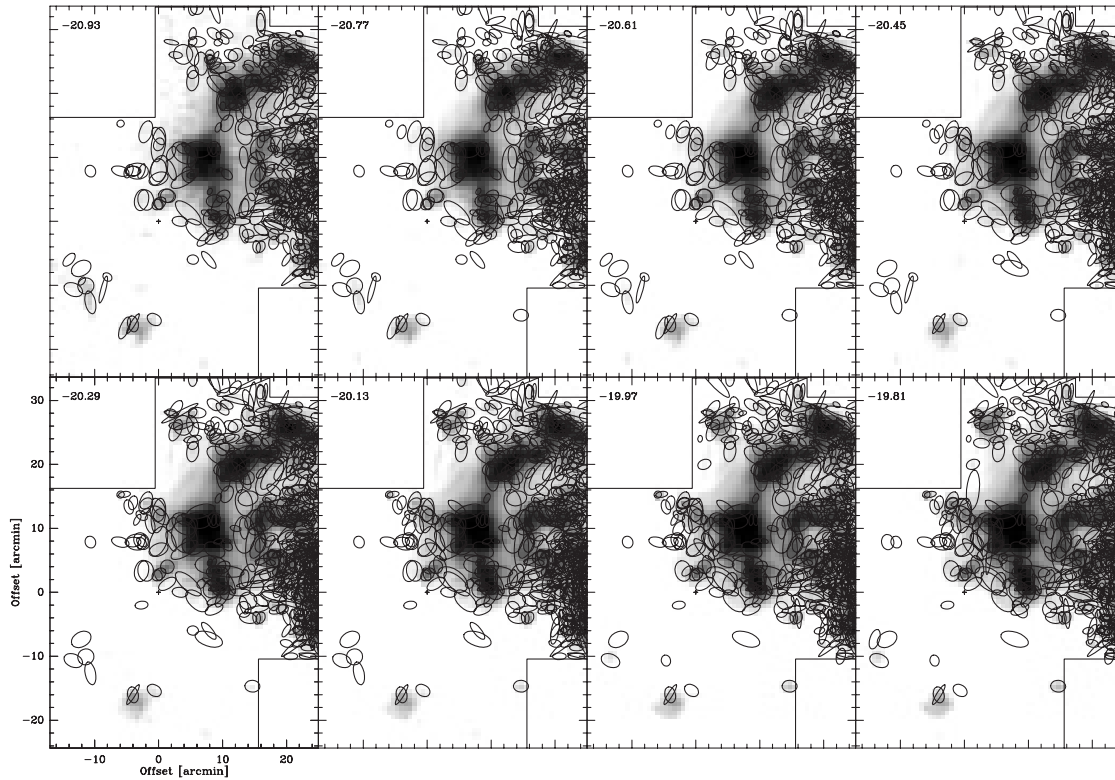

Figure 4   Channel maps of $^{12}CO\ J = 1 \to 0$ line emission in greyscale, starting at the 3σ level in the velocity range -20.9 to $-19.8\,\mathrm{km\,s^{-1}}$ in $0.16\,\mathrm{km\,s^{-1}}$ steps which is equal to the velocity resolution of the data. The ellipses indicate the positions of clumps found with GAUSSCLUMPS.

Table 1.   **Summary of the clump mass distribution analysis of the Carina clouds obtained with** GAUSSCLUMPS **and** CLUMPFIND. **(1) Mapsize. (2) Total mass of the cloud as the sum of the individual clumps found. (3) Virial mass of the cloud determined by Eq. (3) using the line width of the positionally averaged** $^{12}CO\ J = 1 \to 0$ **spectrum and the effective radius $= \sqrt{(area/\pi)}$. (4) Average hydrogen density. (5) Clump mass spectral index. (6) and (7) Mass of the lightest and heaviest clump found. (8) Radius of the most massive clump**

	(1) Area [pc^2]	(2) Total mass [M$_\odot$]	(3) Virial mass [M$_\odot$]	(4) $\langle n(H_2)\rangle$ [10^3 cm^{-3}]	(5) α	(6) M_{low} [M$_\odot$]	(7) M_{high} [M$_\odot$]	(8) R [pc]
GAUSSCLUMPS	884	133 000	751 000	0.16	1.95	1.9	10 000	3.25
CLUMPFIND	884	146 300	751 000	0.40	1.82	3.9	5500	2.4

that 35% of the observed ^{13}CO emission was not identified into clumps. The GC algorithm, on the other hand, finds a much larger number of smaller and lighter clumps (even with masses $\ll 10\,\mathrm{M}_\odot$) but has the tendency to assign additional smaller clumps to the residuals of the previous Gaussian fit, producing a steeper mass spectrum. This effect has to be separated from the real small scale structure found in molecular clouds, for instance protostellar cores with masses of a few $\mathrm{M}_\odot$ and sizes of <0.1 pc.

One possible way to investigate this problem is to observe the same cloud with telescopes of different angular resolutions and to perform a GC analysis to produce a common clump mass spectral distribution. This was done by Schneider et al. (1998) for Rosette, also a bright GMC, and by Heithausen et al. (1998) for a quiescent
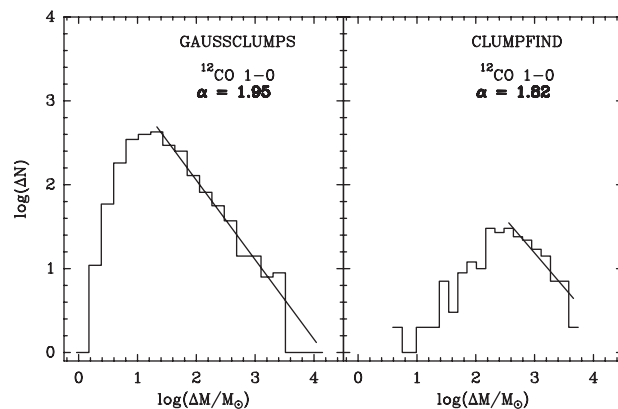
cloud (Polaris Flare). In both cases, the clump mass distributions are continuous. This finding shows that the turnover point in the lower angular resolution data set is not of physical significance but is due to the limited spatial resolution.

The total masses (sum of the individual clumps) derived with both methods do not differ (both around $140\,000\,\mathrm{M}_\odot$). The virial mass, determined by Eq. (3) using the line width of the positionally averaged ^{12}CO $J = 1 \rightarrow 0$ spectrum ($11\,\mathrm{km\,s}^{-1}$) and the effective radius ($\sqrt{(884/\pi)} = 16.8$ pc), is $751\,000\,\mathrm{M}_\odot$. This is a factor of about five higher than the total mass determined by both algorithms. Even considering the large uncertainties in the determination of masses this finding indicates that the Carina cloud as a whole is not self-gravitating.

6 Physical Properties

6.1 Line Width–Size and Mass–Size Relation

A large number of studies of molecular clouds have examined the relationship between a cloud's internal velocity dispersion σ (calculated by Eq. (4)), density $n(\mathrm{H}_2)$, mass M, and size R. In particular, the line width–size relation (Larson 1981) has been tested frequently (e.g. Myers 1983; Solomon et al. 1987) and a power law correlation of the form $\sigma \propto R^{(0.2-0.5)}$ was found to exist. However, the scatter amongst the index is large, typical values range between e.g. 0.21 (Brand et al. 2001), 0.24 for Cepheus OB3 (Carr 1987), 0.42 for L1630 (Lada et al. 1991), 0.49 for Orion A (Tatematsu 1999), 0.5 (Solomon et al. 1987), and 0.53 (Brand & Wouterloot 1995). Some studies, however, did not find such a relation (Loren 1989; Zimmermann & Ungerechts 1990; Simon et al. 2001).

We plot the velocity dispersion σ [$\mathrm{km\,s}^{-1}$] and the mass M [$\mathrm{M}_\odot$] against radius R [pc] in Fig. 6, determined from

Figure 5 The clump mass spectrum of the Carina clouds derived from Mopra ^{12}CO $J = 1 \rightarrow 0$ observations and using the algorithm GAUSSCLUMPS (left) and CLUMPFIND (right), showing the number of clumps dN in the mass interval dM. The best fit to the power law function $\mathrm{d}N/\mathrm{d}M \propto M^{-\alpha}$ is indicated as a straight line.
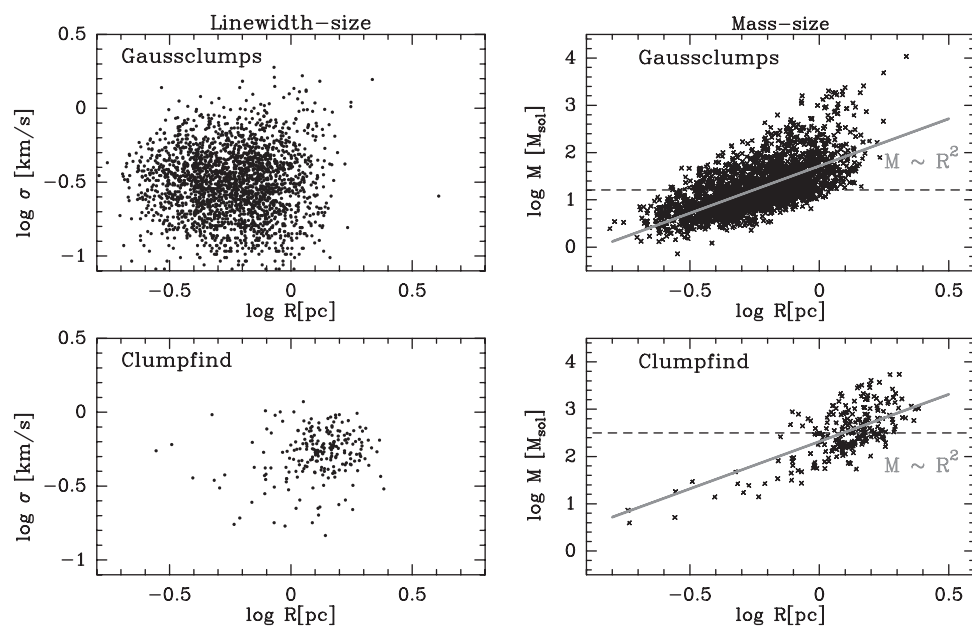

Figure 6 Left: Line width–size relation of the clumps found by GAUSSCLUMPS (top) and CLUMPFIND (bottom). Right: Same plot for the mass–size relation of the clumps. The grey line indicates the Larson relation $M \propto R^2$.

the clumps found by GAUSSCLUMPS (top) and CLUMPFIND (bottom). Generally, the velocity dispersion of the GC is larger (0.1–$2\,\mathrm{km\,s^{-1}}$) than that of the CF clumps (0.2–$1.25\,\mathrm{km\,s^{-1}}$). This finding is surprising, since CF detects spatially more extended and massive clumps than GC so that one would expect a larger velocity dispersion. There is no common relation between clump size and velocity neither for the GC clumps nor for the CF clumps.

For the mass–size relationship of the clumps, we included all clumps with masses above the minimum detectable mass and indicated the turnover mass with a long-dashed line. It should be noted, however, that clumps with masses below this turnover mass are not 'artificial'. To a certain extent they still represent the small scale structure of the material even if they are undersampled (see Section 5.4). The grey line indicates the power law relation $M \propto R^2$ which fits acceptably the CF distribution (bottom). A least-squares fit of the data points yields a slope of (2.34 ± 0.15). For the GC clumps, this line defines only a regime of clumps with radii $<1\,\mathrm{pc}$ ($\log(R) = 0$) and masses roughly between 1 and $50\,\mathrm{M_\odot}$ ($0 < \log(M) < 1.7$). For higher masses and larger radii the slope is steeper. From this plot, it becomes obvious that both algorithms trace rather different regimes of clumps: Within the mass range $\sim 10^2$–$10^4\,\mathrm{M_\odot}$, the CF clumps are generally larger than the GC clumps. At lower masses, only a few clumps covering all radii are found by CF.

6.2 The 'Equilibrium' State of Molecular Clumps

There is a controversial discussion whether molecular clouds as a whole can reach a state of dynamical equilibrium. While e.g. Ballesteros-Paredes et al. (1999) or Elmegreen (2000) argues that clouds are transient features, confined only by a turbulent flow of the interstellar medium, other authors (e.g. Rees 1986) see clouds as stable objects in gravitational equilibrium. A way to characterise the equilibrium state of a cloud or cloud fragment is to determine the virial parameter α_v which measures the ratio of kinetic to gravitational energy density (Bertoldi & McKee 1992):

$$\alpha_v = \frac{1161\sigma^2 R}{M} \qquad (6)$$

Figure 7 shows the virial parameter for all clumps identified by GC (top) and CF (bottom) as a function of mass. The long-dashed line indicates again the turnover mass limit for GC ($10\,\mathrm{M_\odot}$) and CF ($400\,\mathrm{M_\odot}$), respectively. For values $\alpha_v \simeq 1$, the clumps are gravitationally bound and are stabilised by internal thermal and turbulent pressure and magnetic pressure against collapse. Clumps with $\alpha_v > 1$ are externally bound, i.e. 'pressure-confined', or transient features. The short-dashed line ($\log(\alpha_v) = 0$) in the figure indicates the border between the two physical states. Typical values of the virial parameter for GMCs are about $\log(\alpha_v) = 1.3$–1.4 (McKee & Tan 2003). The grey line indicates that α_v goes as the mass to the $-2/3$ power for pressure-confined clumps. This proportionality arises when α_v is written in terms of the Jeans mass M_J
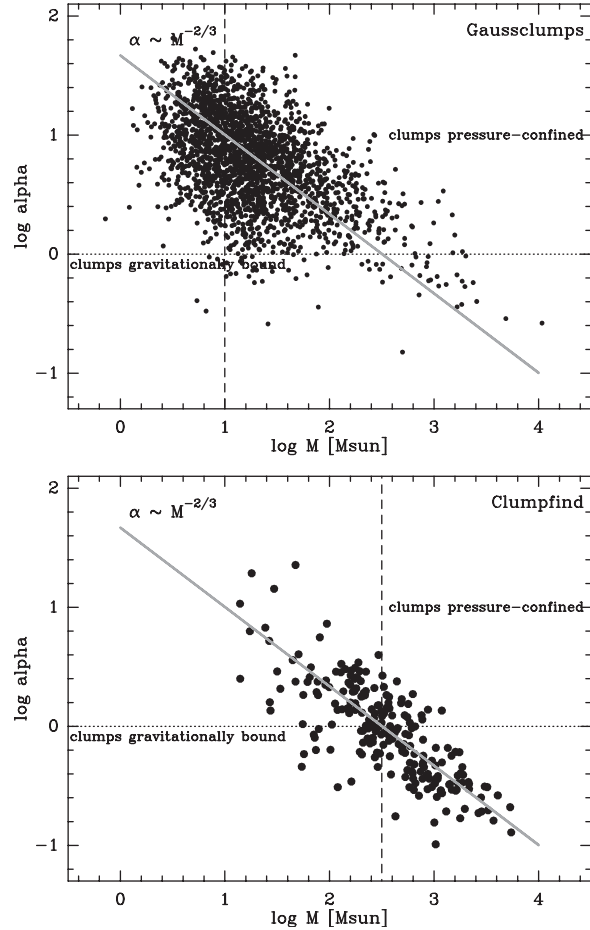

Figure 7 Virial parameter α_v as a function of mass, plotted for the clumps found by GAUSSCLUMPS (top) and CLUMPFIND (bottom). The horizontal short-dashed line indicates $\alpha = 1$ (clumps gravitationally bound) and the vertical long dashed-line the turnover-mass limit of the two algorithms. The grey line indicates the proportionality $\alpha \propto M^{-2/3}$ valid for pressure-confined clumps.

(Bertoldi & McKee 1992) with $\alpha_v \propto 2.9(M_J/M)^{2/3}$ and implies that for pressure-confined clumps, the Jeans mass is not correlated with the masses of the clumps and thus self-gravity is not important. We see that $\alpha_v \propto M^{-2/3}$ does not hold for the regime of gravitationally bound clumps found by GAUSSCLUMPS but holds for the ones found by CLUMPFIND. This is surprising since the most massive clumps are strongly self-gravitating and should thus not fulfill the correlation for pressure-confined clumps (Bertoldi & McKee 1992).

It becomes evident that the most massive clumps ($\log(M) > 2.5$) found by both methods are predominantly gravitationally bound. For $1.5 < \log(M) < 2.5$, about half of the CF clumps and nearly all GC clumps are pressure confined. For masses $\log(M) < 1.5$, all clumps found by both algorithms are stabilised by an external pressure or they are transient. Rathborne et al. (2002) found, by eye-inspection, small and light clumps (12 and $90\,\mathrm{M_\odot}$) in the Carina Keyhole Nebula region which are also not gravitationally bound. They suggest that these clumps represent remains of the original cloud and are now photoevaporating. However, these clumps might not be

Table 2. Properties of some GMCs (column 1). Columns 2 and 3 give the distance and mapsize, columns 4 and 5 the total and virial masses of the clouds. Column 6 denotes the hydrogen density averaged across the cloud and column 7 the UV flux in the associated PDR. α in column 8 is the clump mass spectral index

	Distance [kpc]	Area [pc^2]	Total mass [$10^5\,M_\odot$]	Virial mass [$10^5\,M_\odot$]	$\langle n(H_2)\rangle$ [cm^{-3}]	UV-flux in PDR [$10^3 G_\circ$]	α	Reference
Carina	2.2	884	1.5	5.3	160	10	1.95	This paper
Orion A	0.45	1400[1]	1.04[1]	1.44	500	100[2]	2.1	Nagahama et al. (1998); Bally et al. (1987); Maddalena et al. (1986)
Orion B	0.4	930	0.83–1	0.72[1]	200–460	0.6[3]	1.7	Kramer et al. (1996); Maddalena et al. (1986)
Rosette	1.6	2200	0.8–1.6	2.2	30	0.1–1	1.6	Williams et al. (1995)
GRS[4]	6.0	2640	3.4–4.9	12.6	80		1.8	Simon et al. (2001)
W51	6.7	2000	12.0		25			Carpenter & Sanders (1998)
S35	6.8	700	1.5		160			Saito et al. (1999)
Centaurus	6.9	2000	6.9		160			Saito et al. (2001)
Vela	8.5	810	5.5		490			Yamaguchi et al. (1999)
W49	11.4	1520	3.2–4.8	10.2	160	100	1.6	Simon et al. (2001)

[1] Maddalena et al. (1986).   [2] Orion KL.   [3] NGC2024.   [4] GRSMC 45.46+0.05.

representative for all clumps in the cloud since they are under the influence of the H{\sc ii} region.

7 Discussion

7.1 Comparison to Other GMCs

Large-scale surveys of GMCs are available now for regions within the solar neighborhood, the outer Galaxy (Heyer et al. 2001), and the inner Galaxy (Simon et al. 2001). The environmental conditions differ significantly both globally (influence of galactic rotation and spiral wave compression, overall galactic UV field, metallicity) and locally (e.g. star-formation acticity, internal/external heating sources, evolutionary state of the cloud). A comparison of the Carina Molecular Cloud to other massive, star-forming GMCs may yield information about the general properties of this type of clouds.

Table 2 shows the spatial extent, masses, average H$_2$ densitites and incident UV field in a number of typical GMCs. The inner galaxy clouds (W49 and GRSMC 45.46+0.05) and S35 are similar in mass to the Carina cloud while the Orion clouds and Rosette are lighter, W51 and Vela are a factor of four more massive. There is no clear correlation between mass, density, and clump mass spectral index α.

W49 is the most luminous star-formation region in the Galaxy. Simon et al. (2001) found that the majority of the clumps in W49 are gravitationally bound — in contrast to the Carina clumps which are mainly pressure-bound — which they explain by a high star-formation rate. The clump mass spectral index is slightly flatter for W49 which is probably caused by the larger distance to W49 (11 kpc) since unresolved clumps are blended together and are confused with a single high-mass clump.

The Rosette Molecular Cloud (RMC) is exposed to a much weaker UV field compared to Carina and the average density is much lower. The total mass of the RMC is lower or similar to the mass of Carina (depending on the CO/H$_2$ conversion factor for Rosette) and the clump mass spectrum is flatter. As in Carina, where the OB clusters Tr 14 and Tr 16 have a huge impact on the surrounding gas because their ionising Lyman alpha UV photons together with stellar winds evaporate and disperse molecular clumps, forming proplyds or pillars (Brooks et al. 2003), the Rosette cloud shows signs of an evolved GMC as well. The stellar winds of the Rosette OB cluster NGC 2244 created a central cavity and features like cometary globules and elephant trunks, which are remnants of dense clumps, now photoevaporate or form stars (Schneider et al. 1998).

The archetypical GMCs with star formation activity — Orion A and B — have a similar areal extent, mass, and density compared to Carina. The majority of the clumps in the Orion clouds are not pressure bound. The virial mass is a factor of eight higher than the mass calculated by CO although Maddalena et al. (1986) found that CO and virial masses are the same. Kramer et al. (1996) find that only the southern part of the Orion B cloud as a total is gravitationally bound.

Summarising these findings and considering the large scatter among the parameters derived by different authors in various line tracers, we conclude that there is no significant difference between the GMCs in the solar neighborhood concerning global parameters like average density and clump mass spectral index.

7.2 The Cloud's Physical Parameters: GAUSSCLUMPS versus CLUMPFIND

The physical parameters (e.g. scaling relations, virial parameter) determined individually from both clump identification algorithms and presented in Section 6 are not consistent. No line width–size relation was found using both algorithms and only the CF clumps show a mass–size relation. The virial parameter indicates that nearly all GC clumps are pressure confined or transient whereas the majority of CF clumps are gravitationally bound. Since a number of other recent studies of molecular clouds (see

references from Section 6.1) did not find any or only a weak line width (mass)–size relation, the question rises as to how valid scaling relations are in general since they probably (also) depend on the clump identification procedure.

The scaling law $M \propto R^2$ is valid for a hierarchical and fractal model of molecular clouds (Falgarone & Puget 1986). Some authors (Kegel 1989; Scalo 1990; Ballesteros-Paredes & Mac Low 2002), however, argue that the apparent mass–size relation is due to the observations and/or the analysis process: Any cutoff in column density N, due to the limited dynamic range and/or the minimum intensity level defined by clump finding algorithms, automatically implies $M \propto R^2$, since $M \propto nR^3 \propto (NR^{-1})R^3 \propto R^2$ where n is the density. In this context, GAUSSCLUMPS seems to be less affected by this problem since it spawns a larger range of column densities. Generally, molecular line maps in low-J ($J_{\mathrm{up}} < 4$) CO lines, analysed by eye-inspection or with algorithms selecting local emission peaks defined by a minimum emission level, arrive at this conclusion (see Mac Low & Klessen 2004 for a detailed discussion). Heyer et al. (2001) argue that the line width–size relation is only valid for high-density gas tracers like CS, HCN, and NH$_3$ (Myers 1983). Dense clumps and cores observed in these lines are not readily detected in low-J CO emission due to the smaller critical density. In CO, only lower density, spatially and kinematically extended gas is detected. In addition, velocity superposition of clumps — which turns out to be the most critical factor for determining the physical properties of clumps (Ballesteros-Paredes & Mac Low 2002) — is drastically reduced by using high density tracers.

The existence of the line width–size relation seems to be clearer, even though not observed in all clouds. From a theoretical point of view, a value of $\sigma = 0.33$ for the line width–size relation corresponds to the Kolmogoroff law, describing turbulent diffusion in an incompressible fluid. A value of 0.5 is given by Chiéze (1987) for clouds close to gravitational instability when they interact with a constant pressure environment. Mac Low & Klessen (2004) argue that the relation is a result of the energy spectrum in a supersonic turbulent flow, since larger scales contain more energy and thus produce the observed relation between velocity dispersion (characterised by the line width) and size. In any case, the line width–size relation does not neccessarily imply virialization of the cloud (Combes 1991; Mac Low & Klessen 2004). It is not clear why both algorithms do not show a line width–size relation. We do not think it is due to the fact that we used ^{12}CO as a tracer since other studies, performed in ^{13}CO, equally did not show such a relation (e.g. Loren 1989; Simon et al. 2001).

8 Conclusions

The key point of this paper was to investigate the spatial and kinematic structure of the Carina Northern and Southern molecular cloud by analysing an extended ^{12}CO

$J = 1 \rightarrow 0$ data set taken with Mopra. By applying different clump identification methods (GAUSSCLUMPS and CLUMPFIND) to the data, we determined the clump mass spectral index and investigate the Larson scaling relations (line width–size and mass–size).

The molecular line data show a complex spatial and kinematical structure of the clouds. Two major components were identified — the massive and extended Northern cloud and the Southern cloud which is confined to a dark dust lane which bisects the nebula at optical wavelengths. In between, η Car and the Keyhole Nebula led to the destruction of the original molecular cloud with only a few small molecular clumps remaining (Cox & Bronfman 1995; Brooks et al. 2000; Rathborne et al. 2002).

The clump mass spectral index was found to be 1.95 derived from GC and 1.8 from CF but the population of clumps found is rather different. While CF is only sensitive to a small ($\sim$200) population of spatially extended and massive clumps (which have no substructure) GC detects smaller and lighter clumps as well which constitute a large part of the clump mass spectrum (the total number of clumps found is $\sim$2000). While the majority of clumps found with CF are gravitationally bound, most of the GC clumps are in pressure equilibrium, i.e. they might be transient features. In contrast to that, the clumps of the massive star-forming GMC W49 (Simon et al. 2001) are predominantly gravitationally bound and the mass spectrum is flatter which might be due to a higher star-formation rate in W49. This may imply that evolved star forming regions like Carina generally consist mainly of gravitationally unbound clumps which are photoevaporating with time.

No line width–size relation was found using both algorithms. A mass–size relation with $M \propto R^{2.34}$ was found only for the CLUMPFIND clumps which is probably due to the cutoff limit in column density implied by the minimum level chosen for the clump identification. It was shown by, e.g., Ballesteros-Paredes & Mac Low (2002) that it is basically the velocity distribution of molecular clumps along the line of sight which determines the observed structures in molecular line (channel) maps — in particular in ubiquitous lines like CO — and not the density distribution. Accordingly, only observations tracing high-density molecular lines with a sufficiently large dynamic range and high spatial and velocity resolution are meaningful to investigate molecular cloud structure.

The apparent finding that molecular clouds are in virial equilibrium — as was stated by a number of molecular line studies — is also not necessarily compatible with the physical reality. GMCs are disturbed by dynamical activity (star formation, supernovae or other sources of energy input, rotation) and effects of magnetic fields and (in most of the cases) Galactic disk tidal effects. It is not likely that these phenomena occur on times scales shorter than a possible virialised state of the cloud (see Mac Laren et al. 1988 for a general discussion of the applicability of the virial theorem). It also still remains unclear whether molecular clumps are stable (self-gravitating) physical entities or whether they represent only a temporary stage within a

certain evolution scheme. Therefore, generally valid scaling relations for all types of molecular clouds are rather unlikely anyway. In addition, different physical situations (turbulence, fractal or non-fractal cloud structure, etc.) result in different scaling laws.

We therefore come to a similar conclusion as other authors (e.g. Kegel 1989; Scalo 1990; Mac Low & Klessen 2003) before: observational data sets, each with a limited spatial resolution and dynamic range and/or its selective use at only one resolution and sensitivity together with the application of analysing algorithms and models may lead to a falsified picture of the physics and structure of molecular clouds.

Acknowledgments

References

Ballesteros-Paredes, J., Vazquez-Semadeni, E., & Scalo, J. 1999, ApJ, 512, 286

Ballesteros-Paredes, J., & Mac Low, M. 2002, ApJ, 570, 734

Bally, J., Langer, W., Stark, A., et al. 1987, ApJ, 312, L45

Bertoldi, F., & McKee, C. 1992, ApJ, 395, 140

Blitz, L., & Williams, J. P. 1997, ApJ, 488, L145

Brand, J., & Wouterloot, J. G. A. 1995, A&A, 303, 851

Brand, J., Wouterloot, J. G. A., Rudolph, A. L., & de Geus, E. J. 2001, A&A, 377, 644

Brooks, K. J., Whiteoak, J. B., & Storey, J. W. V. 1998, PASA, 15, 202

Brooks, K. J., Burton, M. G., Rathborne, J. M., et al. 2000, MNRAS, 319, 95

Brooks, K. J., Cox, P., Schneider, N., et al. 2003, A&A, 412, 751

Carpenter, J. M., & Sanders, D. B. 1998, AJ, 116, 1856

Carr, J. S. 1987, ApJ, 323, 170

Chiéze, J.-P., & Pineau Des Forets, G. 1987, A&A, 183, 98

Combes, F. 1991, ARA&A, 29, 195

Cox, P., & Bronfman, L. 1995, A&A, 299, 583

Dame, T. M., Koper, E., Israel, F. P., & Thaddeus, P. 1993, ApJ, 418, 730

Elmegreen, B. G. 2000, ApJ, 539, 342

Elmegreen, B. G., & Falgarone, E. 1996, ApJ, 471, 816

Feinstein, A. 1995, RevMexAA (Serie de Conferencias), 2, 57

Falgarone, E., & Puget, J. L. 1986, A&A, 162, 235

Fukui, Y., Onishi, T., Abe, R., et al. 1999, PASJ, 51, 751

Genzel, R. 1999, Saas-Fee Course 21, ed. D. Pfenniger (Berlin: Springer)

de Graauw, T., Lidholm, S., & Fitton, B. 1981, A&A, 102, 257

Grabelsky, D. A., Cohen, R. S., Bronfman, L., & Thaddeus, P. 1988, ApJ, 331, 181

Heithausen, A., Bensch, F., Stutzki, J., et al. 1998, A&A, 331, L65

Heyer, M. H., & Tereby, S. 1998, ApJ, 502, 265

Heyer, M. H., Carpenter, J. M., & Snell, R. L. 2001, ApJ, 551, 852

Kaufman, M. J., Wolfire, M. G., Hollenbach, D. J., & Luhman, M. L. 1999, ApJ, 527, 795

Kegel, W. H. 1989, A&A, 225, 517

Klessen, R., Burkert, A., & Bate, M. R. 1998, ApJ, 501, L205

Klessen, R., & Burkert, A. 2001, ApJ, 549, 386

Kramer, C., Stutzki, J., & Winnewisser, G. 1996, A&A, 307, 915

Kramer, C., Stutzki, J., Röhrig, R., et al. 1998, A&A, 329, 249

Lada, E. A., Bally, J., & Stark, A. A. 1991, ApJ, 368, 432

Larson, R. B. 1981, MNRAS, 194, 809

Loren, R. B. 1989, ApJ, 338, 902

Mac Laren, I., Richardson, K. M., & Wolfendale, A. W. 1988, ApJ, 333, 821

Mac Low, M., & Klessen, R. S. 2004, RvMP, in press

Maddalena, J., Moscowitz, J., Thaddeus, P., & Morris, M. 1986, ApJ, 303, 375

Mc Kee, C. F., & Tan, J. C. 2003, ApJ, 585, 850

Megeath, S. T., Cox, P., Bronfman, L., & Roelfsema, P. R. 1996, A&A, 305, 296

Motte, F., André, P., & Neri, R. 1998, A&A, 336, 150

Myers, P. 1983, ApJ, 270, 105

Nagahama, T., Mizuno, A., Ogawa, H., et al. 1998, AJ, 116, 336

Price, S. D. 1995, SSRv, 74, 81

Rathborne, J. M., Burton, M. G., Brooks, K. J., et al. 2002, MNRAS, 331, 85

Rees, M. J. 1986, MNRAS, 218, 25

Saito, H., Tachihara, K., Onishi, T., et al. 1999, PASJ, 51, 819

Saito, H., Mizuno, N., & Morigichi, Y. 2001, PASJ, 53, 1037

Salpeter, E. E. 1955, ApJ, 121, 161

Scalo, J. 1990, Physical Processes in Fragmentation and Star Formation, pp. 151–176 (Dordrecht: Kluwer)

Schneider, N., Stutzki, J., Winnewisser, G., et al. 1998, A&A, 335, 1049

Simon, R., Jackson, J. M., Clemens, D. P., et al. 2001, ApJ, 551, 747

Smith, N., Egan, M. P., Carey, S., et al. 2000, ApJ, 532, L145

Solomon, P. M., Rivolo, A. R., Barret, J., et al. 1987, ApJ, 319, 730

Strong, J., Bloemen, J., Dame, T., et al. 1988, A&A, 207, 1

Stutzki, J. 1993, Reviews in Modern Astronomy, 6, pp. 209–232

Stutzki, J., & Güsten, R. 1990, ApJ, 356, 513

Tapia, M., Roth, M., Vázquez, R. A., & Feinstein, A. 2003, MNRAS, 339, 44

Tatematsu, K. 1999, Proc. of Star Formation, 72

Testi, L., & Sargent, A. 1998, ApJL, 508, 91

Williams, J. P., de Geus, E. J., & Blitz, L. 1994, ApJ, 428, 693

Ward-Thomnpson, D. 2002, Science, 295, 76

Williams, J. P., Blitz, L., & Stark, A. 1995, ApJ, 451, 252

Williams, J. P., & Blitz, L. 1998, ApJ, 494, 657

Yamaguchi, N., Mizuno, N., Saito, H., et al. 1999, PASJ, 51, 791

Yamaguchi, N., Ezawa, H., & Kawabe, R. 2003, IAU, 221, 236

Zhang, X., Lee, Y., Bolatto, A., & Stark, A. A. 2001, ApJ, 553, 274

Zimmermann, T., & Ungerechts, H. 1990, A&A, 238, 337